Biomaterials 34 (2013) 5226–5235

Contents lists available at SciVerse ScienceDirect

Biomaterials

journal homepage: www.elsevier.com/locate/biomaterials

Sentinel lymph node imaging by a fluorescently labeled DNA tetrahedron

Kyoung-Ran Kim [a,c,1], Yong-Deok Lee [a,1], Taemin Lee [d], Byeong-Su Kim [d], Sehoon Kim [a,b,*], Dae-Ro Ahn [a,b,*]

[a] The Center for Theragnosis, Biomedical Research Institute, Korea Institute of Science and Technology, Hwarangno 14-gil 5, Seongbuk-gu, Seoul 136-791, Republic of Korea
[b] KIST campus, University of Science and Technology (UST), Hwarangno 14-gil 5, Seongbuk-gu, Seoul 136-791, Republic of Korea
[c] Department of Chemistry, College of Science, Yonsei University, Republic of Korea
[d] School of NanoBioscience and Chemical Engineering, Ulsan National Institute of Science and Engineering (UNIST), Ulsan 689-798, Republic of Korea

ARTICLE INFO

Article history:
Received 23 January 2013
Accepted 23 March 2013
Available online 12 April 2013

Keywords:
Sentinel lymph node
DNA tetrahedron
In vivo imaging
Cancer
Biocompatibility

ABSTRACT

Sentinel lymph nodes (SLNs) are the first lymph nodes which cancer cells reach after traveling through lymphatic vessels from the primary tumor. Evaluating the nodal status is crucial in accurate staging of human cancers and accordingly determines prognosis and the most appropriate treatment. The commonly used methods for SLN identification in clinics are based on employment of a colloid of radionuclide or injection of a small dye. Although these methods have certainly contributed to improve surgical practice, new imaging materials are still required to overcome drawbacks of the techniques such as inconvenience of handling radioactive materials and short retention time of small dyes in SLNs. Here, we prepare a fluorescence-labeled DNA tetrahedron and perform SLN imaging by using the DNA nanoconstruct. With a successful identification of SLNs by the DNA nanoconstruct, we suggest that DNA tetrahedron hold great promises for clinical applications.

© 2013 Elsevier Ltd. All rights reserved.

1. Introduction

Sentinel lymph nodes (SLNs) are the first lymph nodes which cancer cells reach after traveling through lymphatic vessels from the primary tumor. Evaluating the nodal status is crucial in accurate staging of human cancers and accordingly determines prognosis and the most appropriate treatment [1]. While patients with breast cancer and melanoma are currently subject to invasive sentinel lymph node biopsy (SLNB) to stage metastases, alternative noninvasive methods have been pursued. In particular, noninvasive imaging methods based on the blue dyes and radioactive colloids are the major methods for identification of SLNs in clinical research since they were introduced about two decades ago [2,3]. Although these methods are being used widely, there are drawbacks in each method. Owing to the spectral limit of the blue dyes, SLNs cannot be identified without a skin incision [4]. Since the dyes are small sized molecules, they are quickly drained from the initial loading point. This rapid diffusion property, however, becomes disadvantageous for staying in the SLN area surrounded by permeable lymphatic vessels. After short retention in SLN (ca. 15–20 min) [5], the dyes pass to secondary nodes, causing difficulties in distinguishing selectively SLNs from other subsequent nodes. Recently, indocyanine green (ICG), a near infrared (NIR) dye, has been employed to circumvent the optical drawback of the blue dyes [6,7]. While improvement in macroscopic detection of SLNs was achieved by using ICG, the short retention issue could not be addressed since ICG is also a small dye. In contrast to the small dye-based imaging agents, the radioisotope-labeled colloids including the ^{99m}Tc-labeled sulfur colloid have a relatively slow diffusion rate and thus tend to remain at the site of administration [8,9]. Because of this slow diffusion, it takes a long time for the colloids to arrive at a lymph node and should therefore be injected the day before the operation for lymphatic mapping. Additionally, this radioisotope method can be used in limited places because of the safety regulations for radioactive agents. To overcome these drawbacks observed in the conventional dye-guided or radio-guided SLN mapping methods, noninvasive imaging modalities such as ultrasound [10–12], computed tomography (CT) [13,14], magnetic resonance imaging [15–17], optical imaging [18–22], photoacoustic

* Corresponding authors. The Center for Theragnosis, Biomedical Research Institute, Korea Institute of Science and Technology, Hwarangno 14-gil 5, Seongbuk-gu, Seoul 136-791, Republic of Korea.
E-mail addresses: sehoonkim@kist.re.kr (S. Kim), drahn@kist.re.kr (D.-R. Ahn).
[1] K.- R. Kim and Y.-D. Lee contributed equally.

0142-9612/$ – see front matter © 2013 Elsevier Ltd. All rights reserved.
http://dx.doi.org/10.1016/j.biomaterials.2013.03.074

tomography [23–26] have been investigated for identification of SLNs. These newly studied methods utilize mainly nanoparticle-based imaging agents, since they show relatively quick arrival at the lymph node site compared to the colloids of radionuclide and extended retention time at the SLN area compared to the small dyes. Inorganic or polymer nanoparticles, however, have a potential to be toxic *in vivo* since they are made from biologically unnatural materials.

Previously, it has been shown that inherently non-cytotoxic DNA could self-assemble to construct various three dimensional (3D) DNA nanocages including tetrahedra, bipyrimids, octahedra, dodecahedra and fullerene-like structures [27]. Among them, the DNA tetrahedron has been considered one of the most practical DNA nanocages since it can be assembled simply from four DNA strands and prepared in high yield [28,29]. The recent demonstration about cellular uptake of the DNA tetrahedron into mammalian cells has opened a great opportunity for the nanocage to play important roles in biomedical applications [30]. In addition, the tetrahedron is significantly nuclease resistant, which makes the DNA tetrahedron even a more attractive tool for *in vivo* imaging technology [31]. Although previous studies demonstrated that the DNA nanocages could become a promising tool for studying biotechnology such as drug delivery and stimulation of immune response at an *in vitro* cellular level [32,33], *in vivo* applications of the 3D DNA nanoconstructs is still in its infancy. Regarding this, siRNA-loaded DNA tetrahedra were very recently developed and used for effective mRNA regulation in an *in vivo* system as a pioneering study [34].

With high biocompatibility and flexibility for fluorescence modification, the DNA nanoconstructs are promising materials for *in vivo* imaging. In particular, the DNA tetrahedron is likely a good candidate as an SLN imaging agent since its size is within the hydrodynamic diameter required for lymphatic drainage and lymph node retention (6–10 nm) [35]. Here, we prepare a fluorescence-labeled DNA tetrahedron and use it to perform SLN imaging. Retention time at SLNs and specific visualization of the SLNs were estimated to evaluate the imaging efficiency of the DNA nanostructure in the comparison with a corresponding double stranded DNA.

2. Materials and methods

2.1. Preparation of DNA tetrahedron (Td) and DNA duplex (Ds)

All DNA oligonucleotides were purchased from Bioneer (Daejeon, Korea) (Table S1). Td was assembled by mixing S1, S2, S3 and Cy5-S4 (or FAM-S4). Four DNA sequences (250 nM of each sequence) were mixed in TM buffer (10 mM Tris–HCl, 5 mM $MgCl_2$, pH = 8.0). The mixture was denatured by heating to 95 °C and annealed by cooling to 4 °C using a PCR machine (Applied Biosystems, USA). Ds was made from Cy5-S4 and its complementary strand (c-S4) by adopting the same procedure used for assembling of Td.

2.2. Gel electrophoresis

Non-denaturing polyacrylamide gels (6%) were run in TBE buffer with 100 V at 4 °C for 40 min. After electrophoresis, the images were visualized using a fluorescence scanner (Typhoon 9400, GE healthcare, USA).

2.3. Dynamic light scattering

The hydrodynamic size of Td was measured in Zetasizer (Malvern, UK) by following a literature procedure [36].

2.4. AFM imaging

The 100 μL of each DNA samples with specific concentration in buffer solution were spin-coated on a freshly cleaned Si wafer (10 mm × 10 mm) at 2000 rpm for 60 s. DNA Td samples were imaged in a tapping mode on Dimension AFM

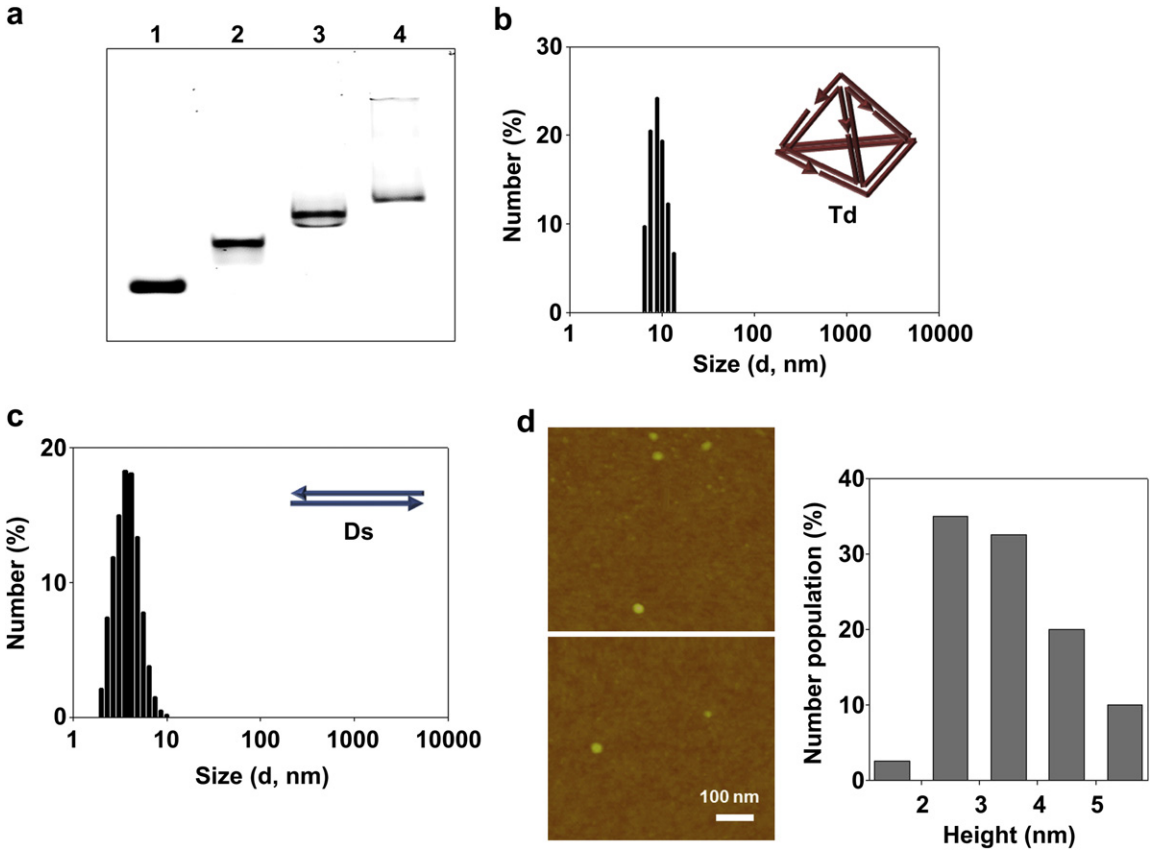

Fig. 1. Characterization of Td. (a) Native PAGE to verify assembly of the tetrahedron. Lane 1: Cy5-S4; Lane 2: Cy5-S4 and S3; Lane 3: Cy5-S4, S3, and S2; Lane 4: Cy5-S4, S3, S2, and S1; DLS data to estimate hydrodynamic sizes of Td (b); and Ds (c); (d) AFM images of Td and height distribution of the Td particles in AFM images.

instrument (Dimension D3100, Veeco, USA) in air, using 0.01–0.025 Ohm·cm antimony (*n*) doped Si probes having a resonance frequency in the range of 332–376 kHz (Veeco-TESP). AFM data were processed with NanoScope 7.20 software.

2.5. SLN mapping by in vivo imaging

The animal study was approved by the animal care and use committee of Korea Institute of Science and Technology and all mice were handled in accordance with institutional regulations. For *in vivo* imaging and disease model preparation, mice were anaesthetized with intraperitoneal injection of 0.5% pentobarbital sodium (0.01 mL/g). Animal disease models were prepared on BALB/c nude mice (male, 5 weeks old, Orient Bio Inc., Korea). Tumors were established by subcutaneous inoculation of SCC7 cells (1.0×10^6 cells suspended in the culture medium) into the thigh of mice. Cy5-Ds and Cy5-Td were intradermally injected into the left forepaw pad. The real-time fluorescence of SLN mapping was recorded using a CCD camera, implemented in a high-sensitivity imaging system (IVIS-spectrum, Perkin–Elmer, USA).

2.6. Ex vivo imaging and histologic analysis

After *in vivo* imaging studies, *ex vivo* near-infrared fluorescence images of resected organs, lymph nodes and the rest of the body were taken by a IVIS-spectrum imaging system with the same acquisition setup as used for the *in vivo* imaging. For optical and fluorescent histologic inspection, DAPI (4′,6′-diamidino-2-phenylindole)-stained sections (20 μm, CM1900 microtome, Leica, Germany) of the OCT-embedded lymph nodes were investigated on microscopes (Leica DMI3000 B, Germany and Nuance Multispectral Imaging System, Perkin Elmer, USA).

2.7. Transfection of Td into RAW264.7 cells

RAW264.7 cells were plated in glass-bottomed 35 mm petri dishes with DMEM media (Gibco, USA) containing 10% heat inactivated fetal bovine serum, 1% penicillin and streptomycin. After 2.5×10^4 cells were seeded in each dish, the dishes were incubated overnight at 37 °C in humidified atmosphere containing 5% CO_2. The growth medium was removed from each cell sample, and the cells were washed twice with PBS (Gibco, USA). Each transfection mixture was made using Td or Ds (250 nM) in the fresh medium (250 μL) without serum and the antibiotics, then added to a sample of cells, and incubated for 6 h at 37 °C in humidified atmosphere containing 5% CO_2. Final concentration of DNA samples was 10 nM.

2.8. Microscopic imaging of Td in RAW264.7 cells

For microscopic examination and flow cytometry analysis, FAM-S4 strand was used for the preparation of fluorescently labeled Td. The nuclei were stained using Hoechst 34580 (3 μg/mL, Invitrogen, USA), and the cells were washed with PBS (200 μL) twice. The cell culture medium (200 μL) was then added. Live cells were imaged using a fluorescence microscopy (DeltaVision, Applied Precision, USA). Excitation/emission filters used for fluorescein and Hoechst 34580 were 480–500/509–547 nm, and 340–380/432–482 nm, respectively.

2.9. Flow cytometry analysis

RAW264.7 cells were seeded on 24-well culture plates at a density of 10^5 cells/mL and cultured for 24 h and then washed twice with PBS. They were incubated with the fluorescently labeled DNA molecules by using the same manner adopted for the

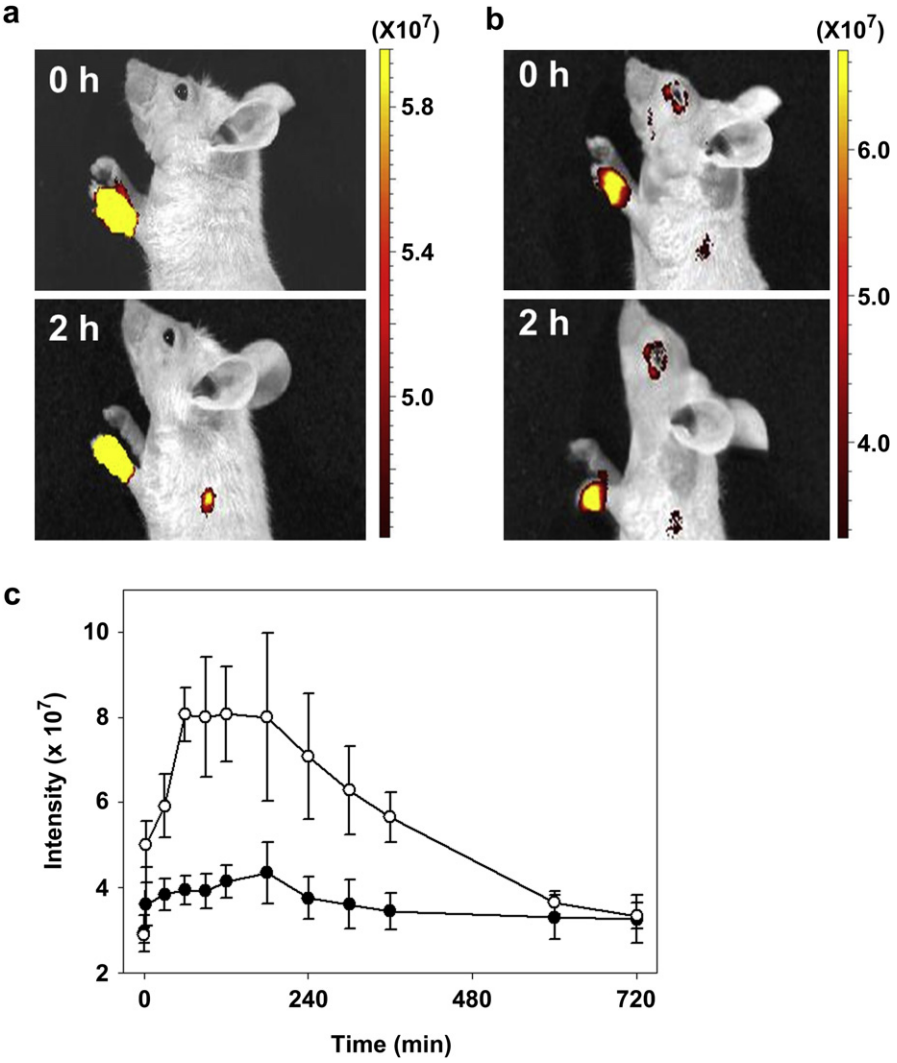

Fig. 2. SLN imaging by the DNA probes. Mouse images just after (top) and 2 h after (bottom) the injection of Cy5-Td (a); or Cy5-Ds (b); (c) Time-dependent intensity changes of Cy5 emission at the SLN area after injection of Cy5-Td (blank) and Cy5-Ds (filled).

transfection experiment, harvested, and washed three times with PBS. Then, 0.2 mL of trypsin replacement (TrypLE™, Gibco, USA) was added to each sample, and the samples were incubated for 5 min at 37 °C. Then 1 mL of the medium was added to each sample, and the resulting cell suspensions were transferred to conical tubes (Falcon™ tubes, BD Biosciences, USA) and centrifuged for 3 min at 2500 rpm. Supernatant was removed, and the cell pellets were resuspended in 1 mL of PBS. Fluorescence intensity of the cells was estimated by flow cytometry (FC500, Beckman coulter, USA). Samples of at least 1000 cells were analyzed in triplicate.

2.10. Fluorescence resonance energy transfer (FRET) analysis

RAW264.7 cells were plated in glass-bottomed 35 mm petri dishes with DMEM media (Gibco, USA) containing 10% heat inactivated fetal bovine serum, 1% penicillin and streptomycin. After 2.5×10^4 cells were seeded in each dish, the dishes were incubated overnight at 37 °C in humidified atmosphere containing 5% CO_2. The growth medium was removed from each cell sample, and the cells were washed twice with PBS (Gibco, USA). Cy3-Td-Cy5 was assembled by mixing Cy3-S1, S2, S3, and Cy5-S4. Cy3-Ds-Cy5 was prepared by mixing Cy3-S1 and Cy5-S4. Mono-labeled control probes for Td and Ds were prepared by mixing Cy3-S1, S2, S3, and S4 (or S1, S2, S3, and Cy5-S4) and S4 and Cy3-S1 (or S1 and Cy5-S4), respectively. The mixtures were denatured by heating to 95 °C and annealed by cooling to 4 °C using a PCR machine. The transfection was performed by using the same manner adopted for the uptake experiment. Final concentration of DNA samples was 100 nM. Then, the cells were washed twice by PBS, and incubated with fresh cell culture (200 μL) at 37 °C, and imaged at different time points (0, 2, 4, 6, 8, and 24 h) using a fluorescence microscopy (Delta Vision). Excitation/emission filters used for Cy3 and Cy5 were and 542–570/594–630 and 630–650/665–705 nm, respectively. For FRET analysis, the signals were recorded using different excitation/emission filters such as Cy3/Cy3 (donor/donor), Cy3/Cy5 (donor/acceptor) and Cy5/Cy5 (acceptor/acceptor) and analyzed by ImageJ.

3. Results and discussion

3.1. Preparation and characterization of Td

The sequences of oligonucleotides to construct the DNA tetrahedron and the linear duplex were as presented in Table S1. The DNA tetrahedron was assembled by following the protocol in the previous literature [28]. Construction of the tetrahedron structure (Td) was analyzed on a non-denaturing polyacrylamide gel electrophoresis (PAGE). The incremental retardation by strand-wise addition of DNA, the typical phenomenon in assembly of DNA tetrahedron, was observed in the PAGE analysis (Fig. 1a). For the size determination, dynamic light scattering (DLS) was measured for the DNA tetrahedron and compared with the linear duplex DNA (Ds). The sizes of the DNA tetrahedron and the DNA duplex were 8.89 (±0.22) nm and 4.19 (±0.39) nm, respectively (Fig. 1b and c). AFM was additionally measured for further characterization, and the sizes of DNA tetrahedron observed in the AFM images were 3–5 nm at the dried state (Fig. 1d and Fig. S1).

To estimate the serum stability of the DNA nanostructures, the nuclease resistance of the Cy5-labeled Td (Cy5-Td) was examined in 10% mouse serum solution. More than 70% of the tetrahedron structure survived after 7 h exposure to the serum solution, whereas complete degradation of linear duplex DNA (Cy5-Ds) was observed after 3 h (Fig. S2). This hour-long serum stability of Td would be an advantageous property for SLN imaging, since the SLN biopsy operation takes about 30 min after visualization of SLNs [37].

3.2. SLN imaging by fluorescently labeled Td

After characterization of the DNA tetrahedron assembly and analysis of its stability in serum, visualization of SLNs was attempted by subcutaneous injection of the Cy5-labeled DNA construct (Cy5-Td) in the forepaw of mice with and without tumor inoculation. Tumor-bearing mice were used to render the experimental condition close to the real disease situation where lymph

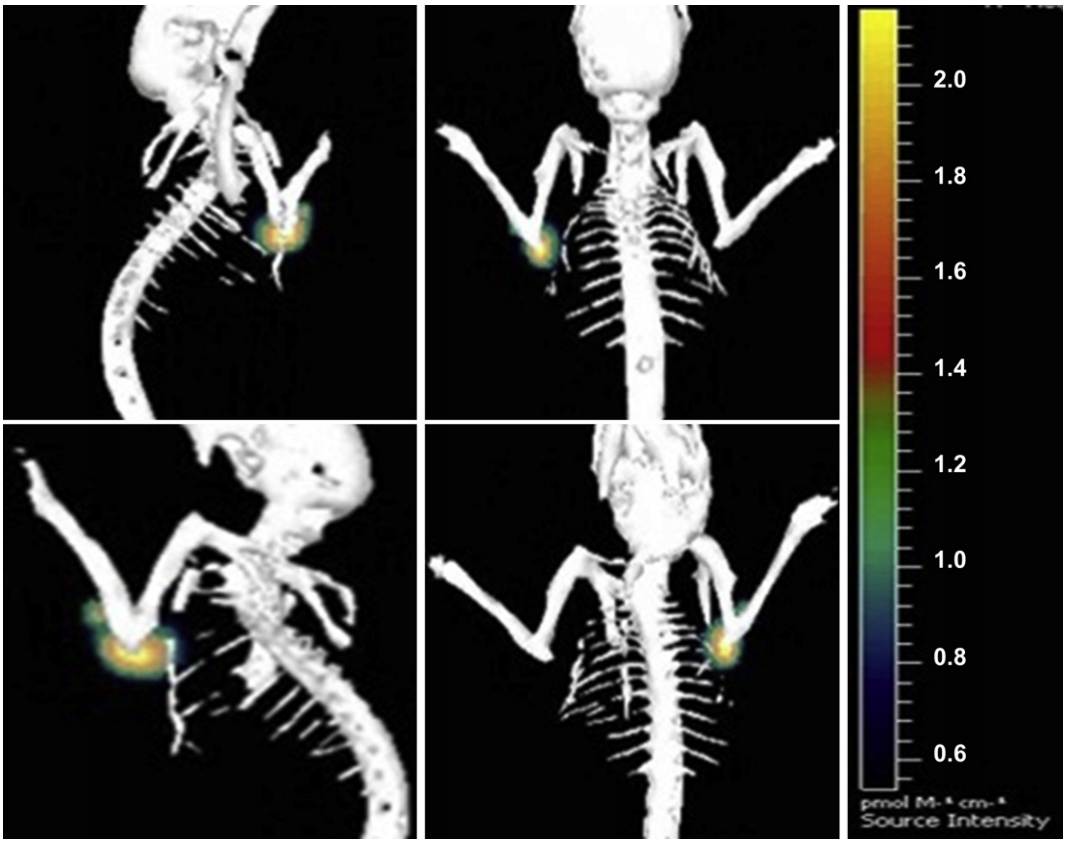

Fig. 3. Optical tomographic images of a Cy5-Td-injected mouse were obtained by the IVIS imaging system. SLNs in the left axillary are specifically visualized by the fluorescence emission of Cy5.

nodes become active and swollen in the presence of tumor [38]. As SLNs of forepaws are usually located in axillary regions, the fluorescence signal through the skin of the axillary region was monitored to assign SLNs. Fig. 2 presents the fluorescence images of tumor-bearing mice after injection of the DNA probes. SLNs in an axillary could be detected successfully by using Cy5-Td as the imaging probe (Fig. 2a), whereas the linear DNA probe, Cy5-Ds showed negligible fluorescence signal in SLNs and failed to provide spatial information of SLNs (Fig. 2b). In contrast to the specific localization of Cy5-Td in SLNs, Cy5-Ds was observed in an undesired region such as face. To obtain kinetic information about SLN imaging by the probes, fluorescence intensity of each probe at the lymph node was quantified (Fig. 2c). The fluorescence intensity level reached to the maximum level at 2 h after the injection of Cy5-Td. The intensity decreased slowly to the background level for the next 8 h. In contrast to the tetrahedron structure, the linear DNA provided the intensity level that was hardly distinguishable from the background signal during the measurement. Compared to non-tumored normal mice (Fig. S3), tumor-bearing mice with active lymph nodes showed notably enhanced SLN entrapment of Cy5-Td with higher intensity and prolonged retention of fluorescence signals. These results suggest that the DNA tetrahedron could be used for SLN imaging and that the nanoparticle-like structure is inevitable for DNA materials to be utilized in the application. The translocation of the Cy5-Td in SLNs of the axillary was additionally demonstrated by the tomographic images of the probe-injected mouse as shown in Fig. 3.

3.3. Evaluation of SLN imaging by ex vivo analysis and histologic analysis

After observing specific SLN imaging by Cy5-Td in live animals (Fig. 4a), biodistribution of the fluorescent DNA tetrahedron was monitored in the mouse sacrificed 2 h after injection. Fluorescence from Cy5 labeled on the DNA tetrahedron indicated that the Cy5-Td probe was accumulated mainly in SLNs, with small amount in the kidney, liver, and spleen (bottom in Fig. 4b). On the contrary, the linear DNA probe, Cy5-Ds exhibited relatively low uptake in SLNs and accumulated similarly to other organs containing the probe (top in Fig. 4b). The difference in the emission spectra between other tissues and SLNs indicated that the distinct fluorescence intensity observed in the SLNs was due to Cy5 labeled on the DNA tetrahedron, which excluded the possibility of non-specific imaging resulting from autofluorescence of the tissues (Fig. 4c and d).

After observing efficient imaging of SLNs by Cy5-Td, the distribution of the DNA constructs in the SLN tissues was investigated by histological analysis of the nodes. The fluorescence intensity of Cy5 in the frozen sections indicated that the majority of Cy5-Td was taken up by cells in the sinusoidal region, which could be identified by the fluorescence emission (Fig. 5a). In contrast, Cy5-Ds was scarcely accumulated in the cells, showing a diffuse and dim staining pattern (Fig. 5b). The relative intensity of the Cy5-Td-treated tissues was about five times higher than that of Cy5-Ds-treated ones which was as low as the control background signal (Fig. S4).

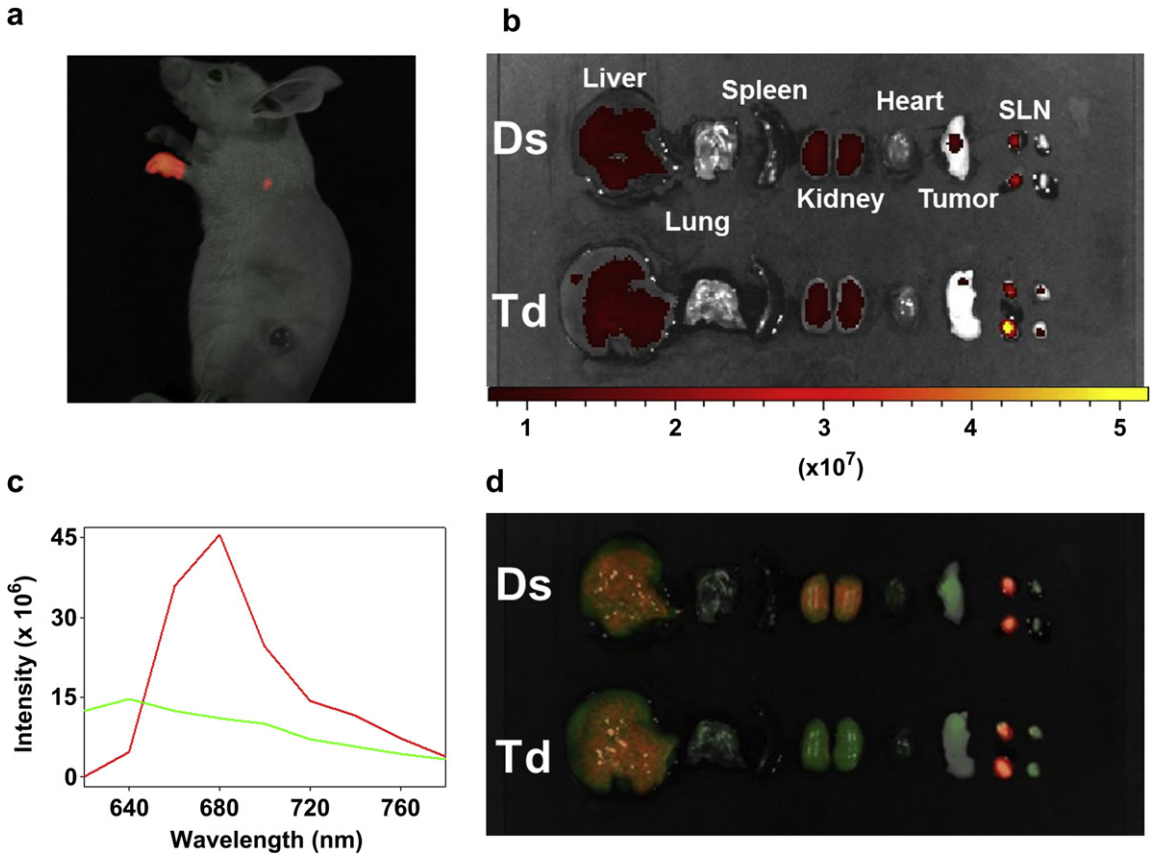

Fig. 4. (a) An *in vivo* fluorescence image taken at 2 h after administration; (b) *Ex vivo* NIR fluorescence images of isolated organs from the Cy5-Ds-injected mouse (top) and Cy5-Td-injected mouse (bottom). Organs are displayed one after another from left to right: livers, lungs, spleens, kidneys, hearts, tumors, SLNs in the left axillary, and SLNs in the right axillary; (c) Un-mixed emission profiles of Cy5 (red) and autofluorescence (green) at SNLs; (d) Un-mixed fluorescence images of isolated organs from the Cy5-Ds-injected mouse (top) and Cy5-Td-injected mouse (bottom) indicate Cy5 emission specifically from SLNs in the left axillary. (For interpretation of the references to color in this figure legend, the reader is referred to the web version of this article.)

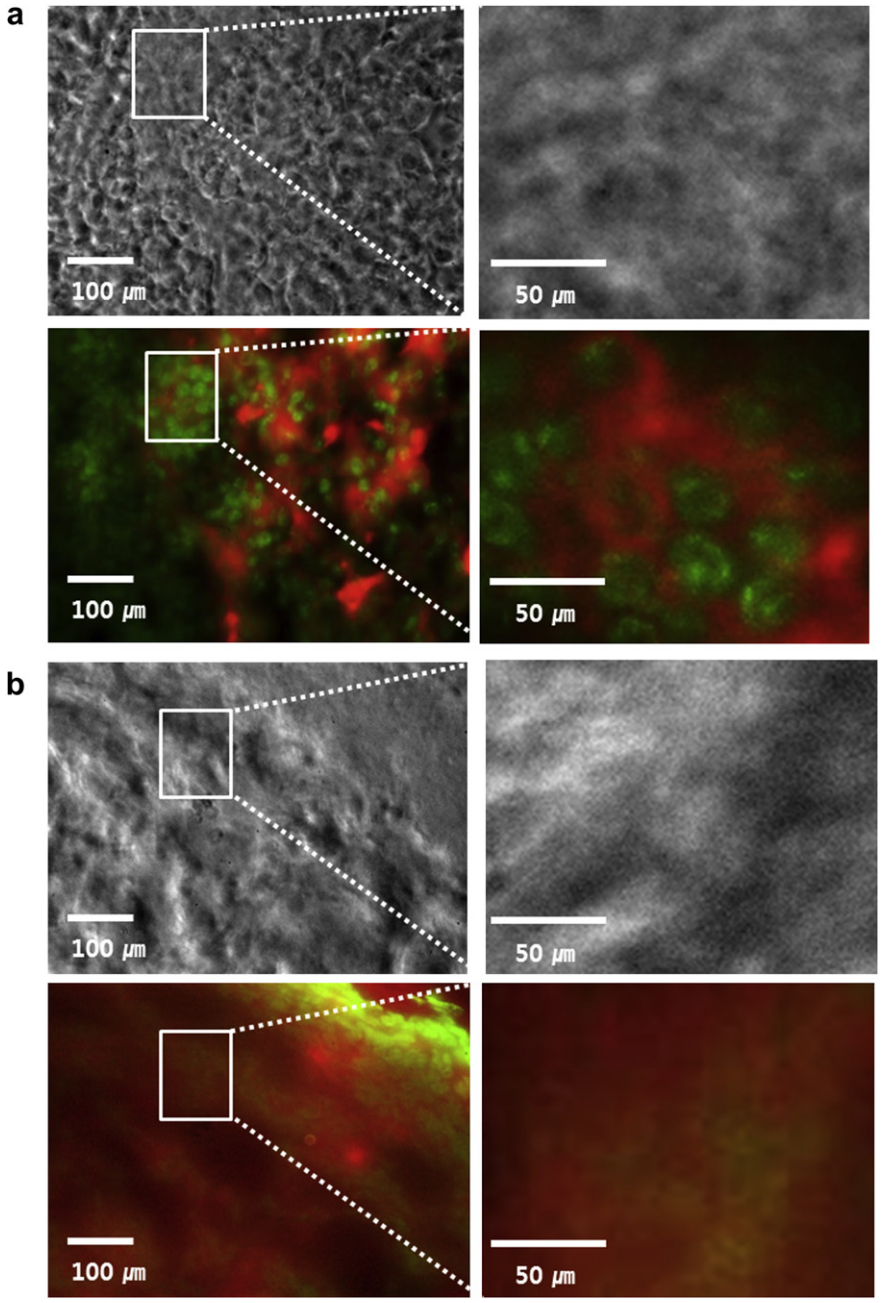

Fig. 5. Fluorescence analysis of the histological localization of Cy-Td (a); and Cy-Ds (b); The zoomed-in images of the squared area in the left panel are shown in the right panel. The bright field images are shown at the top and the corresponding fluorescent images are at the bottom, respectively. Nuclei are stained with DAPI and colored as green. (For interpretation of the references to color in this figure legend, the reader is referred to the web version of this article.)

3.4. Advantageous properties of Td for efficient SLN imaging: improved cellular uptake and intracellular stability

To further examine the cellular internalization of the DNA constructs observed during *in vivo* SLN imaging, *in vitro* studies on cellular uptake of the DNA constructs were also carried out in RAW264.7 mouse macrophage precursor cells. RAW264.7 was chosen as a model system for *in vitro* cellular studies since macrophages are one of various cell types found in lymph nodes [39]. When the fluorescein-labeled DNA tetrahedron was incubated with RAW264.7 cells for 6 h, cytoplasm of the cells became fluorescent under the microscopy suggesting that Td was successfully delivered into the cells (Fig. 6a). The delivery of Ds, however, was not as effective as Td. For quantitative analysis of the uptake of the DNA constructs in cells, the delivery efficiency was analyzed by flow cytometry (Fig. 6b and c). Relatively enhanced delivery of Td was observed compared with Ds, which was consistent with the microscopic images. Although it was highly expected that non-clathrin-mediated endocytosis mechanism are involved with the uptake of Td as previously reported [40], we additionally examined the uptake mechanism for Td in RAW264.7 cells by employing three different endocytosis inhibitors since the cell line we used in the current study were not an identical cell line to the previous cases. As the result, non-clathrin-mediated endocytosis mechanisms played a role also in the delivery of Td into RAW264.7 cells as predicted (Fig. 6d). In terms of cytotoxicity of the DNA tetrahedron,

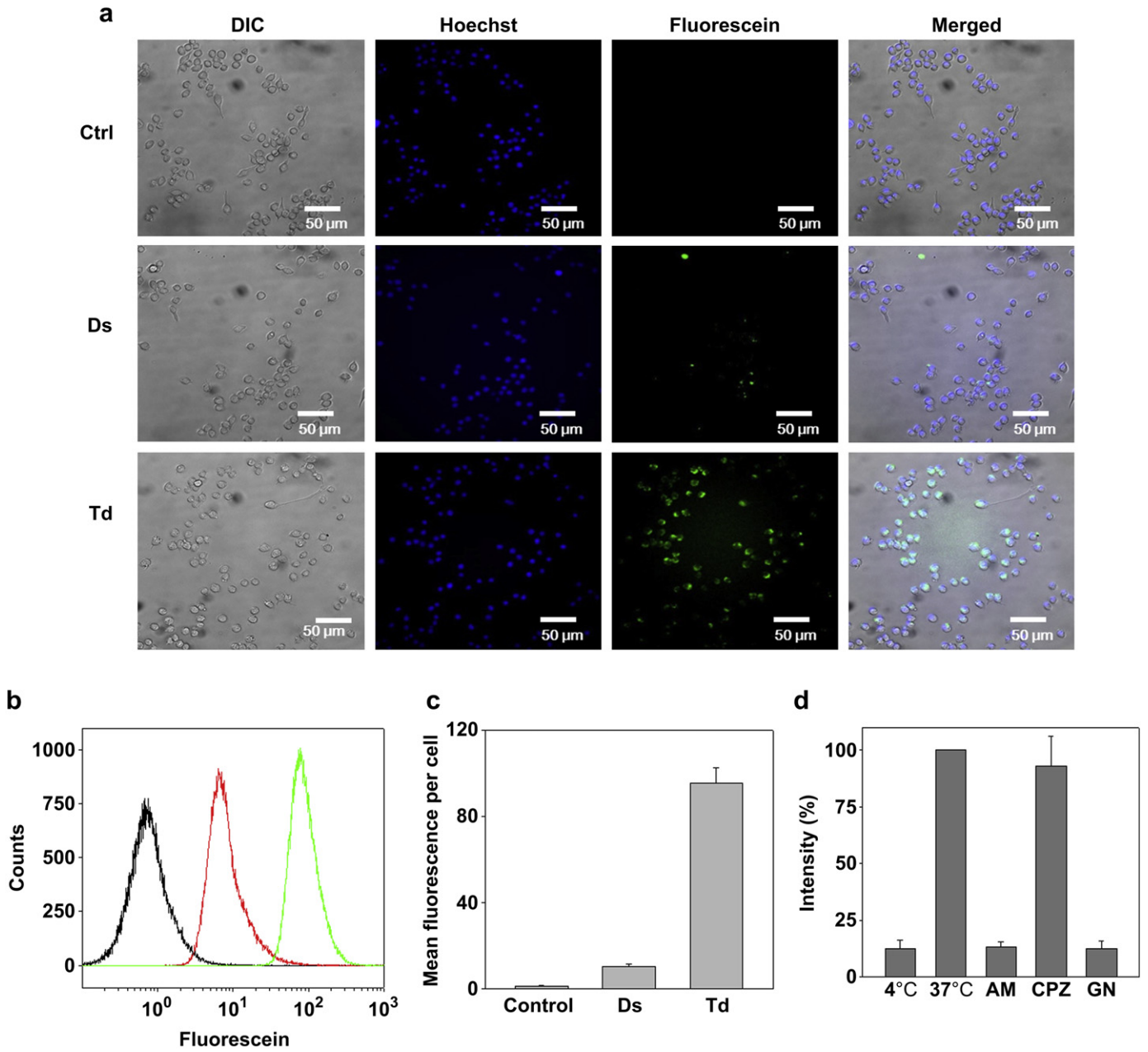

Fig. 6. Cellular uptake of the DNA probes. (a) Fluorescence microscopic images of RAW264.7 cells showing intracellular uptake of Td and Ds; (b) Flow cytometry profiles of the cells treated with Td (green) and Ds (red), compared with that of the untreated control cells (black); (c) Quantitative data showing enhanced cellular uptake of Td compared to Ds. (d) Average cellular fluorescence intensity of Td in RAW264.7 cell lysates from the cells cultured in the presence of three different endocytosis inhibitors: chlorpromazine (CPZ for inhibition of clathrin-mediated endocytosis), amiloride (AM for inhibition of macropinocytosis), and genistein (GN for inhibition of caveolae-mediated endocytosis). Fluorescence intensity is normalized to the total amount of cellular proteins. (For interpretation of the references to color in this figure legend, the reader is referred to the web version of this article.)

Td did not influence on the cell viability, indicating that the DNA nanoconstruct is non-cytotoxic (Fig. S5).

Intracellular stability of the tetrahedron assembly was also investigated by monitoring fluorescence resonance energy transfer (FRET) efficiency of the dually labeled Cy3-Td-Cy5. Emission profiles were obtained after irradiation of the excitation light for the donor on the cells treated with Cy3-Td-Cy5. The FRET signal was monitored as the ratio of increased acceptor intensity at 670 nm to the decreased donor intensity at 580 nm (Fig. 7 and Fig. S6). The intensity of cells treated with the mono-labeled Cy3-Td and Cy5-Td were used as the background controls. Increased concentration of DNA probes (100 nM) was used for fluorescent cellular images. Fig. 7a shows intracellular FRET images of Td at different time points. Although time-dependent decreases were observed not only in Cy3 and Cy5 intensities but also in FRET efficiency, FRET-based signals with about 36% of initial intensity were still observed even after 8 h in the cells treated with Td, showing a considerable intracellular stability of Td consistent with the previous result [31,32]. In contrast, the FRET signal from the linear Cy3-Ds-Cy5 decreased rapidly and reached the quite low level with about 16% of initial intensity after 8 h (Fig. 7b), showing the similar degradation patterns to those observed in the *in vitro* serum

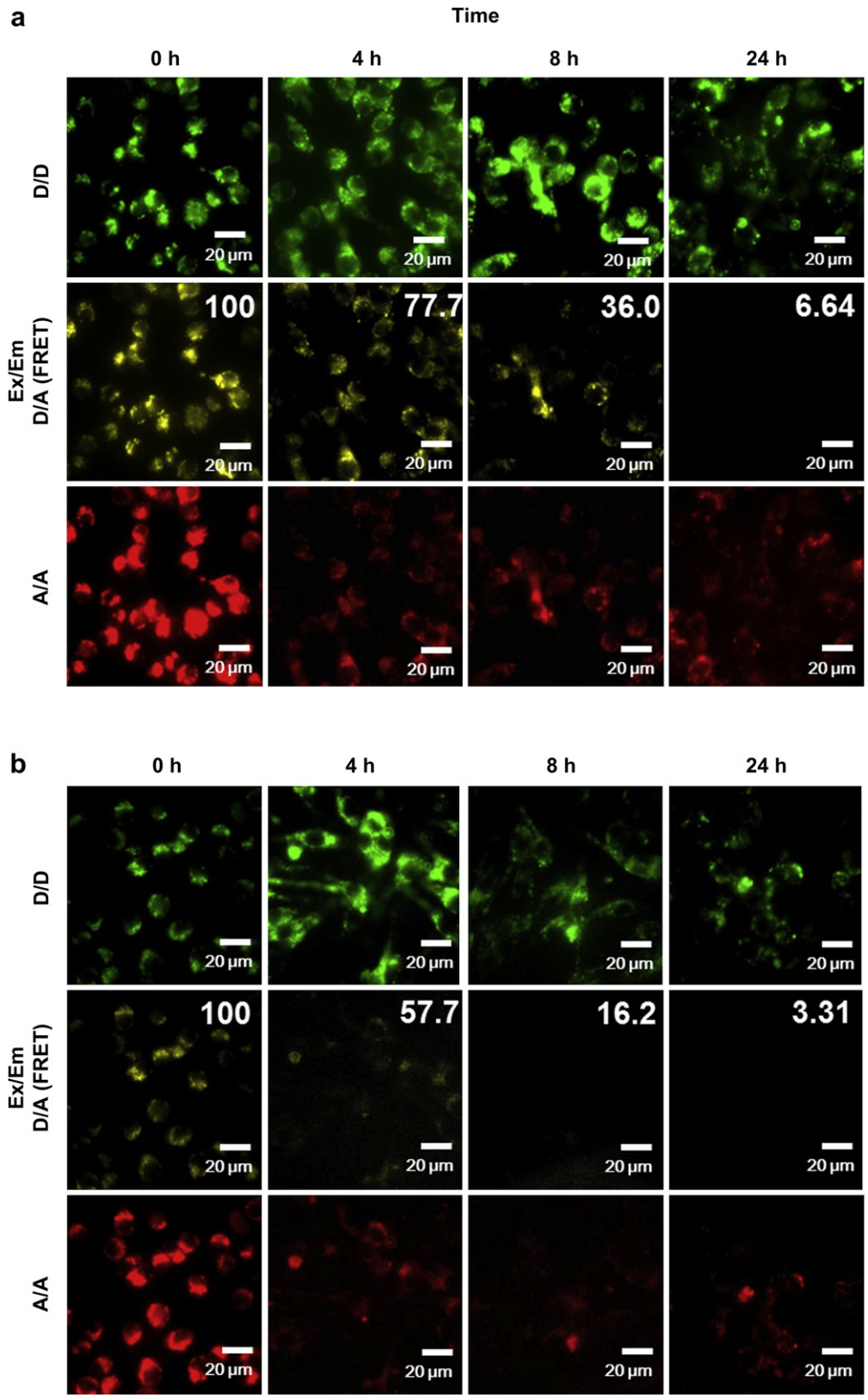

Fig. 7. Intracellular FRET to examine stability of Td (a); and Ds (b); Images obtained by using excitation and emission filters for the donor (Cy3) are presented at the top rows. Images obtained by using the filters for the acceptor (Cy5) are presented at the bottom rows. The normalized FRET signal (%) based on the FRET intensity at the initial state (0 h) is presented at the top-right corner of each FRET image. FRET images obtained by using the excitation filter for the donor and the emission filter for the acceptor are presented at the middle rows. Ex/Em: the excitation filter and the emission filter. D/D: the excitation filter and the emission filter for the donor were used. D/A: the excitation filter for the donor and the emission filter for the acceptor were used. A/A: the excitation filter and the emission filter for the acceptor were used.

stability evaluation (Fig. S2). These results suggest that the successful SLN imaging by the DNA tetrahedron is due to increased cellular uptake and improved intracellular stability of the tetrahedron structure compared to the linear duplex in macrophage cells of SLNs.

4. Conclusions

In this study, we utilized a nano-sized DNA tetrahedron for efficient SLN imaging based on fluorescence of the Cy5 label on the DNA construct. The visualization of SLNs by the dye-labeled DNA nanoconstruct was successfully demonstrated in an *in vivo* model system. Compared with the linear DNA probe, the DNA tetrahedron showed enhanced translocation in SLNs and prolonged retention time at the node. These advantageous properties of DNA tetrahedron for SLN mapping were due to enhanced cellular uptake and intracellular stability of the DNA construct. The efficiency of cellular uptake and the improved intracellular stability of the DNA tetrahedron were evaluated by *in vitro* FRET assays using mouse macrophage precursor cells. Since the DNA tetrahedron is composed of inherently biological molecules that can be degraded into metabolic nucleotides, it is virtually non-cytotoxic, non-immunogenic, and has a low potential to cause safety problems that may be observed in other organic or inorganic nanoparticle-based SLN imaging systems when applied in the clinical area. Moreover, not only the fluorescence label but also chemical moieties for other imaging modalities can be easily and site-specifically incorporated into a DNA strand of the tetrahedron. Therefore, with the successful performance in SLN imaging, the high biocompatibility and the simple preparation with an immense potential for tailor-made modification, the DNA tetrahedron is expected to be a useful SLN imaging agent also in the human clinical model.

Acknowledgment

This study was supported by a grant funded by Korea Institute of Science and Technology, a grant of the Basic Science Research Program through the National Research Foundation of Korea funded by the Ministry of Education (2011-0009172), a grant the Proteogenomic Research Program through the National Research Foundation of Korea funded by the Korean Ministry of Education, Science and Technology, and a grant of the Korea Healthcare technology R&D Project, the Ministry of Health & Welfare, Republic of Korea (A121191).

Appendix A. Supplementary data

Supplementary data related to this article can be found at http://dx.doi.org/10.1016/j.biomaterials.2013.03.074.

References

[1] Torabi M, Aquino SL, Harisinghani MG. Current concepts in lymph node imaging. J Nuc Med 2004;45:1509–18.
[2] Krag DN, Weaver DL, Alex JC, Fairbank JT. Surgical resection and radiolocalization of the sentinel lymph node in breast cancer using a gamma probe. Surg Oncol 1993;2:335–9.
[3] Giuliano AE, Kirgan DM, Guenther JM, Morton DL. Lymphatic mapping and sentinel lymphadenectomy for breast cancer. Ann Surg 1994;220:391–8.
[4] Abe H, Mori T, Umeda T, Tanaka M, Kawai Y, Shimizu T, et al. Indocyanine green fluorescence imaging system for sentinel lymph node biopsies in early breast cancer patients. Surg Today 2011;41:197–202.
[5] Sato K. Current technical overviews of sentinel lymph node biopsy for breast cancer. Breast Cancer 2007;14:354–61.
[6] Kitai T, Inomoto T, Miwa M, Shikayama T. Fluorescence navigation with indocyanine green for detecting sentinel lymph nodes in breast cancer. Breast Cancer 2005;12:211–5.
[7] Tagaya N, Yamazaki R, Nakagawa A, Abe A, Hamada K, Keiichi KK, et al. Intraoperative identification of sentinel lymph nodes by near-infrared fluorescence imaging in patients with breast cancer. Am J Surg 2008;195:850–3.
[8] Tsopelas C. Particle size analysis of (99m)Tc-labeled and unlabeled antimony trisulfide and rhenium sulfide colloids intended for lymphoscintigraphic application. J Nucl Med 2001;42:460–6.
[9] Wilhelm AJ, Mijnhout GS, Franssen EJ. Radiopharmaceuticals in sentinel lymph node detection – an overview. Eur J Nucl Med 1999;26:S36–42.
[10] Vassallo P, Edel G, Roos N, Naguib A, Peters PE. In-vitro high-resolution ultrasonography of benign and malignant lymph nodes: a sonographic-pathologic correlation. Invest Radiol 1993;28:698–705.
[11] Yang WT, Goldberg BB. Microbubble contrast-enhanced ultrasound for sentinel lymph node detection: ready for prime time? Am J Roentgenol 2011;196:249–50.
[12] Krishnamurthy S, Sneige N, Bedi DG, Edieken BS, Fornage BD, Kuerer HM, et al. Role of ultrasound-guided fine-needle aspiration of indeterminate and suspicious axillary lymph nodes in the initial staging of breast carcinoma. Cancer 2002;95:982–8.
[13] Kim J, Lee J, Chang E, Kim S, Suh K, Sul J, et al. Selective sentinel node plus additional non-sentinel node biopsy based on an FDG-PET/CT scan in early breast cancer patients: single institutional experience. World J Surg 2009;33:943–9.
[14] Oh MH, Lee NH, Kim HS, Park SP, Piao Y, Lee JS, et al. Large-scale synthesis of bioinert tantalum oxide nanoparticles for x-ray computed tomography imaging and bimodal image-guided sentinel lymph node mapping. J Am Chem Soc 2011;133:5508–15.
[15] Joshi T, Pankhurst Q, Hattersley S, Brazdeikis A, Hall-Craggs M, De Vita E, et al. Magnetic nanoparticles for detecting sentinel lymph nodes. Eur J Surg Oncol 2007:1135.
[16] Song KH, Kim C, Cobley CM, Xia Y, Wang LV. Near-infrared gold nanocages as a new class of tracers for photoacoustic sentinel lymph node mapping on a rat model. Nano Lett 2009;9:183–8.
[17] Surguladze B, Zhorzoliani R, Tskitishvili T. Novel method of sentinel lymph node detection in malignant tumors using preparation 'unimag'. Breast Cancer Res 2007;9(Suppl. 1):15.
[18] Kim SH, Lim CK, Na JH, Lee YD, Kim KM, Choi KW, et al. Conjugated polymer nanoparticles for biomedical in vivo imaging. Chem Commun 2010;46:1617–9.
[19] Noh YW, Kong SH, Choi DY, Park HS, Yang HK, Lee HJ, et al. Near-infrared emitting polymer nanogels for efficient sentinel lymph node mapping. ACS Nano 2012;6:7820–31.
[20] Kosaka N, Mitsunaga M, Bhattacharyya S, Miller SC, Choyke PL, Kobayashi H. Self-illuminating in vivo lymphatic imaging using a bioluminescence resonance energy transfer quantum dot nano-particle. Contrast Media Mol Imaging 2011;6:55–9.
[21] Cong L, Takeda M, Hamanaka Y, Gonda K, Watanabe M, Kumasaka M, et al. Uniform silica coated fluorescent nanoparticles synthetic method, improved light stability and application to visualize lymph network tracer. PLoS ONE 2010;5:e13167.
[22] Kobayashi H, Ogawa M, Kosaka N, Choyke PL, Urano Y. Multicolor imaging of lymphatic function with two nanomaterials: quantum dot-labeled cancer cells and dendrimer-based optical agents. Nanomedicine (Lond) 2009;4:411–9.
[23] Song KH, Stein EW, Margenthaler JA, Wang LHV. Noninvasive photoacoustic identification of sentinel lymph nodes containing methylene blue in vivo in a rat model. J Biomed Opt 2008;13:054033.
[24] Kim JW, Galanzha EI, Shashkov EV, Moon HM, Zharov VP. Golden carbon nanotubes as multimodal photoacoustic and photothermal high-contrast molecular agents. Nat Nanotechnol 2009;4:688–94.
[25] Akers WJ, Kim C, Berezin M, Guo K, Fuhrhop R, Lanza GM, et al. Noninvasive photoacoustic and fluorescence sentinel lymph node identification using dye-loaded perfluorocarbon nanoparticles. ACS Nano 2010;5:173–82.
[26] Pan D, Cai X, Yalaz C, Senpan A, Omanakuttan K, Wickline SA, et al. Photoacoustic sentinel lymph node imaging with self-assembled copper neodecanoate nanoparticles. ACS Nano 2012;6:1260–7.
[27] Chhabra R, Sharma J, Liu Y, Rinker S, Yan H. DNA self-assembly for nanomedicine. Adv Drug Deliv Rev 2010;62:617–25.
[28] Goodman RP, Schaap AT, Tardin CF, Erben CM, Berry RM, Schmidt CF, et al. Rapid chiral assembly of rigid DNA building blocks for molecular nanofabrication. Science 2005;310:1661–5.
[29] Goodman RP, Berry RM, Turberfield AJ. The single-step synthesis of a DNA tetrahedron. Chem Commun 2004:1372–3.
[30] Walsh AS, Yin HF, Erben CM, Wood MJA, Turberfield AJ. DNA cage delivery to mammalian cells. ACS Nano 2011;5:5427–32.
[31] Keum JW, Bermudez H. Enhanced resistance of DNA nanostructures to enzymatic digestion. Chem Commun 2009:7036–8.
[32] Li J, Pei H, Zhu B, Liang L, Wei M, He Y, et al. Self-assembled multivalent DNA nanostructures for noninvasive intracellular delivery of immunostimulatory CpG oligonucleotides. ACS Nano 2011;5:8783–9.
[33] Chang M, Yang CS, Huang DM. Aptamer-conjugated DNA icosahedral nanoparticles as a carrier of doxorubicin for cancer therapy. ACS Nano 2011;5:6156–63.
[34] Lee HJ, Lytton-Jean AKR, Chen Y, Love KT, Park AI, Karagiannis ED, et al. Molecularly self-assembled nucleic acid nanoparticles for targeted in vivo siRNA delivery. Nat Nanotechnol 2012;7:389–93.

[35] Longmire MR, Ogawa M, Choyke PL, Kobayashi H. Biologically optimized nanosized molecules and particles: more than just size. Bioconjug Chem 2011;22:993–1000.
[36] Afonin KA, Grabow WW, Walker F, Bindewald E, Dobrovolskaia M, Shapiro BA, et al. Design and self-assembly of siRNA-functionalized RNA nanoparticles for use in automated nanomedicine. Nat Protoc 2011;6:2022–34.
[37] Kim MC, Kim HH, Jung GJ, Lee JH, Choi SR, Kang DY, et al. Lymphatic mapping and sentinel node biopsy using 99mTc tin colloid in gastric cancer. Ann Surg 2004;239:383–7.
[38] Nishimura G, Sano D, Tanigaki Y, Taguchi T, Horiuchi C, Matsuda H, et al. Maxillary sinus carcinoma: the only symptom was neck lymph node swelling. Auris Nasus Larynx 2006;33:57–61.
[39] Cynthia L, Willard M. Normal structure, function and histology of lymph nodes. Toxicol Pathol 2006;34:409–24.
[40] Kim K-R, Kim D-R, Lee T, Yhee JY, Kim B-S, Kwon IC, et al. Drug delivery by a self-assembled DNA tetrahedron for overcoming drug resistance in breast cancer cells. Chem Commun 2013;49:2010–2.